Simulation and vibrational analysis of thermal oscillations of single-walled carbon nanotubes

Polina Pine

Russel Berrie Nanotechnology Institute, Technion, Haifa 32000, Israel

Yuval E. Yaish[*]

Department of Electrical Engineering, Technion, Haifa 32000, Israel

Joan Adler

Department of Physics, Technion, Haifa 32000, Israel

The first four flexural thermal vibrational modes of single-walled carbon nanotubes (SWCNTs) of various lengths and radii were studied using atomistic molecular dynamics within the framework of the Brenner interatomic potential and Fourier analysis. These simulations provide clear evidence for the failure of simplistic analytic models to accurately extract resonance frequencies as the ratio R/L between the tube radius and the length increases. They are in excellent agreement with the Timoshenko beam model, which includes the effect of both rotary inertia and of shearing deformation. In addition, our results partially resolve Yakobson's paradox and provide an upper cutoff estimate for the effective SWCNT thickness.

PACS number(s): 62.25.−g

I. INTRODUCTION

Carbon nanotubes (CNTs) posses unique electrical and mechanical properties and are of great interest for both basic and applied research. One active research field is that of nano-electro-mechanical systems (NEMS) based on CNTs. With respect to conventional NEMS, CNTs are extremely light, have very high Young's moduli ($\sim$5TPa), and contain a small amount of structural defects, and it is anticipated that they will oscillate at high frequencies with high quality factors Q. For example, a typical single-walled carbon nanotube (SWCNT) of 100 nm length and 1 nm in diameter has total mass four orders of magnitude smaller than conventional NEMS. Hence, assuming all other properties being equal, CNT resonators are expected to reach the ultimate mass, stress, and pressure sensitivities. These attributes collectively make CNTs suitable for a multitude of technological applications such as ultrafast sensors, actuators, and signal processing components.[1,2]

In the last few years there has been significant progress in experimental measurements of the vibrational modes of SWCNTs, in achieving extremely high quality factors, and in sensing ultralow external masses that adhere to the nanotubes.[3–7] Since the natural frequency is sensitive to the applied external load, one of the principles of sensing is based on the natural frequency shift of a carbon nanotube resonator under an external perturbation. Numerous studies have been made of the vibrational modes of SWCNTs with various external parameters, using molecular dynamics (MD) simulations,[8–13] continuum mechanics models,[14–16] and structural mechanics approaches.[17,18] Their objectives were to estimate the elastic constants of CNTs, such as Young's (E) and shear (G) moduli, Poisson's ratio (ν), and the effective CNT thickness (h).

Estimates for Young's modulus of carbon nanotubes are scattered in the literature, ranging between 1 and 6 TPa.[15,17,19,20] This scattering is known as Yakobson's paradox.[21] Huang *et al.*[22] assert that this range is a result of the scattering of the estimates for the thicknesses of the nanotube. They obtain an analytical expression for the tube thickness, and therefore the elastic moduli, and demonstrate their dependence on the type of loading, e.g., uniaxial tension or uniaxial stretching, as well as on the nanotube radius R and chirality when $R < 1$ nm. They also showed that the thickness of graphene is dependent on the interatomic potential. A complementary analytical model by Wang and Zhang[23] took the different approach of measuring h and hence E, but while these calculations certainly shed light on Yakobson's paradox they do not completely address the issue of modeling the frequency dependence of nanotube vibrations on radius and length. Both these studies were based on a continuum model. However, as the specimen size diminishes, the discrete structure of the material can no longer be homogenized into a continuum, because the nanotube thickness will also vary as a function of its vibrational modes (n) near the places where it is more sharply bent or extended. Therefore, we suspect that the entire picture may be more complex. Since knowledge of the frequency dependence on length, radius, and loading is essential to progress toward deeper understanding and technological applications, we have made extensive, carefully equilibrated molecular dynamics (MD) simulations of SWCNTs and now present a precise analysis of their vibrations. Our high quality data for the thermal vibrations were decomposed into different modes, and the dependence of the four lowest modes on the lengths and radius of the nanotube was calculated. After describing our approach and results we will compare them with the predictions of two continuum mechanics models of beams. We will conclude with a discussion of agreements and discrepancies in light of Yakobson's paradox and the Huang *et al.*[22] results.

II. SIMULATION DETAILS AND RESULTS

The Brenner interatomic potential[24] and the predictor corrector algorithm were selected for the MD. The Brenner interatomic potential is an analytic potential energy function

for solid carbon and hydrocarbon molecules based on a reactive bond order (REBO) formalism which allows covalent bond breaking and creation with associated changes in atomic hybridization within a classical potential. Being empirically derived (by fitting to data sets from experiments and to *ab initio* calculations) it does not treat electrons explicitly or include any explicit quantum effects. However, it is transferable to different carbon hybridizations and allotropes and we selected an extended version that has been well verified for fullerenes and nanotubes.[25–27] The length of runs needed for the vibrational analysis excludes the possibility of using an approach that treats electrons explicitly or even within a tight-binding approximation; thus this potential is an optimal choice. It is equivalent to Sec. I of Ref. 22. Moreover, the potential's extension to hydrocarbon molecules will greatly simplify the modeling of vibrational changes when additional molecules are adsorbed on the SWCNT, as we plan to carry out in the future. Our code is applicable to nanotubes of any radius and length, and the nanotube is resilient to deformations far larger than those it experiences here. Throughout the code development we generated still and animated atomic images with AViz[28] for verification purposes.

In Fig. 1(a) we show a (7,7) SWCNT, with a single period (28 atoms here) drawn in Fig. 1(c). The axis of the nanotube is in the *Y* direction, and we study vibrations in the *Z* direction. (Our validation process included confirming identical (within statistical error) results for vibrations in the *X* direction.) Different boundary conditions were explored, but for the purposes of recording vibrations for analysis and comparison with beam equations the nanotubes were clamped at both ends, by freezing the first (last) three periods as shown in Fig. 1(b) (where only the left half of the tube was drawn).

A large number of SWCNTs with different lengths and radii were studied, and in order to reduce the amount of data needed for the vibrational analysis we selected some special points where data were recorded. The centers of mass [spheres inside the nanotube in Fig. 1(a)] for each period were identified, making up a line of points which we call the centered axis (CA). The center of mass (CM) of the entire nanotube [large sphere in Fig. 1(a)] falls in the middle of this line. Since at the CM the $n = 2,4$ amplitudes vanish, we monitored vibrations near the CM of the 10th period, which is about $1/4$ of the way along the SWCNT, indicated by the asterisk (∗) in Figs. 1(a) and 1(b).

Two different thermodynamic ensembles were tested: canonical and microcanonical. No substantial difference in frequency values was found and we present the canonical ensemble results below. In order to keep temperature constant a Berendsen thermostat[29] was applied. To ensure stable nanotube structure and eliminate intrinsic tension, we collected data after a period of slow initial thermalization to 300 K (periodic boundary conditions with no frozen edges) waiting until the length of the equilibrated nanotube remained constant up to insignificant fluctuations. In order to obtain adequate statistics for all vibrational modes we let every nanotube vibrate 1000 times more than the period of its lowest frequency, using a MD time step of 0.5 fs. We then applied a fast Fourier transform (FFT) analysis to the data at several points (including one near the CM) to calculate the power as a function of
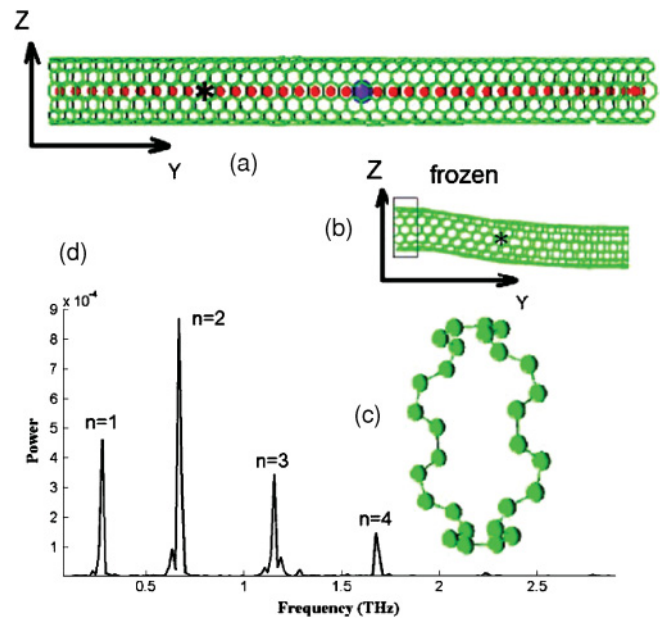

FIG. 1. (Color online) (a) Single-walled carbon nanotube (green), with the CA made up of the centers of mass of each period of the nanotube as (red) spheres inside the nanotube, and a (blue) large atom to indicate its CM. The asterisk (∗) marks one place where all the first four modes have finite amplitude. (b) Vibrating nanotube with clamped ends (only the left half of the tube was drawn). (c) One period of a (7,7) SWCNT. The images are generated with AViz.[28] (d) FFT analysis of the first four thermal vibrational modes ($n = 1$–4) in the *Z* direction at a point near the center of mass of the 30th period at 300 K.

frequency for each nanotube. Figure 1(d) depicts the frequency as a function of the power of the vibrational modes after the FFT for the shortest nanotube (98.38 Å) at the point indicated by the asterisk in Figs. 1(a) and 1(b), about 1.42 Å from the CM of the 10th period. As expected, at this point the second mode had the highest amplitude and the fourth had the lowest.

We initially investigated the effect of the length on the vibrational frequencies, building (7,7) SWCNTs with lengths (*L*) of 98.38, 147.57, 196.76, 245.95, and 295.14 Å with a diameter (=2*R*) of 9.5 Å. Due to the fact that three last/first periods are frozen the vibrating fragments of the nanotubes are 83.62, 132.81, 182.00, 231.19, and 280.38 Å long, respectively. In Fig. 2 we show the frequencies of the first four modes as a function of the length of the nanotube (the plus signs, circles, asterisks, and squares are for modes 1–4, respectively).

We also simulated the frequencies of the first four modes as a function of nanotube radius. We changed the aspect ratio to create different nanotubes of fixed 98.38 Å length. Nanotubes of the following chiral vectors and radii were tested: (3,3) *R* = 2.0 Å, (5,5) *R* = 3.39 Å, (7,7) *R* = 4.75 Å, (9,9) *R* = 6.10 Å, (11,11) *R* = 7.46 Å, and (14,14) *R* = 9.49 Å. Again the three last/first periods were frozen giving a vibrating fragment of 83.62 Å. Figure 3 depicts frequency values as a function of tube radius where the same mode notation as for Fig. 2 was used.
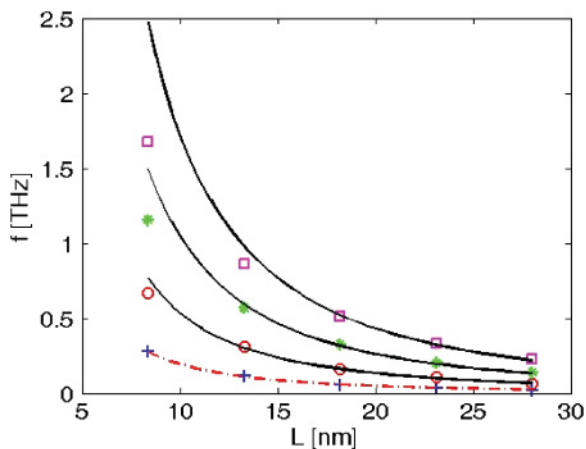
FIG. 2. (Color online) First four vibrational modes as a function of length. The plus signs, circles, asterisks, and squares are for modes 1–4, respectively, and the continuous and dashed-dot lines are derived from Eq. (3).

III. COMPARISON WITH A SIMPLE CONTINUUM MODEL

The oscillation motion of NEMS based on CNTs is often described via continuum mechanics, where SWCNTs are modeled as continuous beams[30] or shells[15] with fixed wall thickness h and fixed Young's modulus E.[31,32] Typically the "tube length"/"tube radius" (L/R) aspect ratio is very large, and the SWCNT may be regarded as homogenous beam with the same cross section and elastic properties. A continuous, homogeneous, isotropic, linear elastic beam whose properties do not vary along its length will obey the Euler-Bernoulli beam equation

$$EI\frac{\partial^4 u}{\partial y^4} - T_0\frac{\partial^2 u}{\partial y^2} = -\rho A_m \frac{\partial^2 u}{\partial t^2} = \omega^2 \rho A_m u, \qquad (1)$$

where $I = \pi R h(4R^2 + h^2)/4$ is the moment of inertia, u is the transverse beam displacement (in our case, in either the x or z direction), T_0 is the residual tension, and ρ is the density, with a cross sectional area of $A_m = 2\pi R h$ and angular frequency
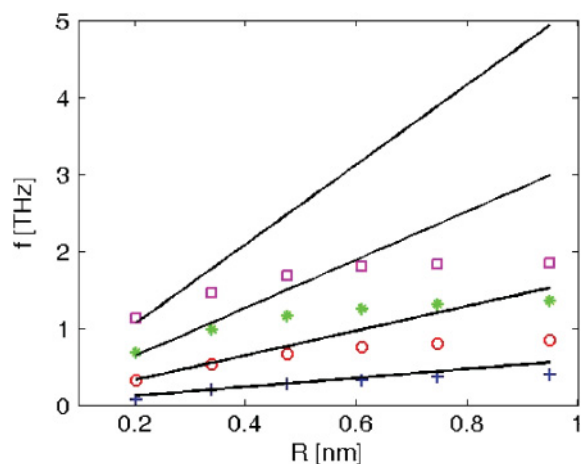

FIG. 3. (Color online) First four vibrational modes as a function of radius. The plus signs, circles, asterisks, and squares are for modes 1–4, respectively, and the continuous lines are derived from Eq. (3).

ω. One can perform the following transformation, $y = \xi L$, for the dimensionless parameter ξ and Eq. (1) becomes

$$\frac{\partial^4 u}{\partial \xi^4} - \frac{L^2}{L_0^2}\frac{\partial^2 u}{\partial \xi^2} = \frac{\partial^4 u}{\partial \xi^4} - \frac{1}{p^2}\frac{\partial^2 u}{\partial \xi^2}$$
$$= \frac{\omega^2 \rho A_m L^4}{EI}u = \beta^4 u. \qquad (2)$$

$L_0^2 = EI/T_0$, $p = L_0/L$, and $\beta^4 = \omega^2 \rho A_m L^4/EI$. β is a parameter whose importance becomes apparent when boundary conditions will be imposed. Equation (2) has an analytical solution and for appropriate boundary conditions the resonance frequencies can be found. For $T_0 = 0$, and the boundary condition of a beam clamped at both ends, the solution for Eq. (2) for the first four modes yields $\beta_n^0 = 4.73, 7.85, 10.99, 14.13$, respectively.[31] Knowing β_n^0 gives the resonance frequencies of

$$f_n^0 = \frac{(\beta_n^0)^2}{2\pi}\sqrt{\frac{EI}{\rho A_m}}\frac{1}{L^2}. \qquad (3)$$

Equation (3) predicts that the frequency depends linearly on tube radius and has a length dependence of $1/L^2$, assuming that R, h, ρ, and E are constant. Figures 2 and 3 depict detailed comparisons between the simulated data and Eq. (3). Initially, a best fit for the first mode of Fig. 2 was derived, and very good agreement was obtained (dashed-dot red line in Fig. 2). It is worth mentioning that the mass per unit length was calculated directly by counting the number of carbon atoms per unit cell in these armchair tubes and then multiplying it by the number of unit cells in one meter, and not by using the approximate value given by the density ρ. The bending rigidity EI turns out to be $EI = (6.7 \pm 0.6) \times 10^{-26}\,\mathrm{Nm}^2$, and from Eq. (3) one may obtain the anticipated higher vibrational modes for the different tube lengths. These results are plotted with continuous black lines in Fig. 2. Since EI depends on the tube radius, the bending rigidity for the second set of data presented in Fig. 3 was calculated using ratios between various moments of inertia. For that purpose a tube thickness h of 0.66 Å was assumed.

From both figures it is clear that for small $\mu = R/\lambda_n$, where λ_n is the wavelength of the nth mode, the Euler-Bernoulli (EB) beam model predicts the natural frequencies as well as the higher vibrational modes of SWCNTs very well. Moreover, for $h = 0.66$ Å and Poisson's ratio $\nu = 0.4$, it gives a tension rigidity $Eh/(1 - \nu^2) = 236\,\mathrm{GPa \cdot nm}$, which is in excellent agreement with the calculated tension rigidity from Huang et al.[22] However, as μ increases the deviations from the classical beam model become more and more significant and alternative models should be considered. One simplified model can allow for the Young's modulus to be varied over the different lengths and tube radii as long as Eq. (3) is satisfied. The result of such an analysis is shown in Fig. 4, where the ratio of the calculated bending rigidity to $(EI)_0$ at small μ is plotted as function of μ. The circles and plus signs correspond to the f vs L and the f vs R data, respectively. One can notice that most of the data are scattered along some imaginary line that starts around 1 and drops down to a fifth of its initial value as μ increases. The significant drop starts around $\mu \simeq 0.05$ and by examining each point separately together
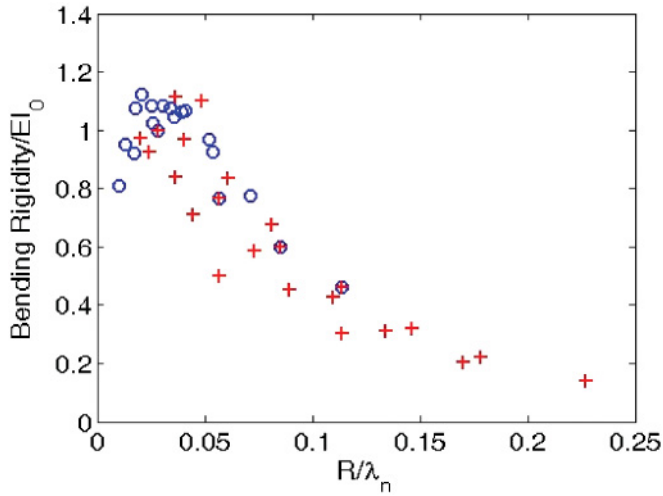
FIG. 4. (Color online) Relative bending rigidity versus $\mu = R/\lambda_n$. The circles and plus signs correspond to the f vs L and the f vs R data, respectively.

with its corresponding location in Fig. 2 or 3 one can observe that for points below $\mu \simeq 0.05$ the agreement with the EB model is very good, but above this value it becomes poorer, as μ increases. Although several theoretical studies predict the radius dependance of the bending rigidity,[17,22,33] the overall change is expected to be smaller than that presented in Fig. 4.

IV. EXTENDED MODEL AND DISCUSSION OF RESULTS

One way to proceed further is to abandon the beam model of SWCNTs and adopt the shell model[15] in order to explain the simulated data. However, since in the limit of small μ, the EB beam model coincides very well with the data, it would be beneficial to extend this model to larger μ. An extension of the EB beam model for larger μ is known as the Timoshenko beam model[34] which takes into account shear deformation and rotational inertia effects, making it suitable for describing the behavior of short beams, in the limit when the wavelength approaches the thickness of the beam. Physically, taking into account the added mechanisms of deformation effectively lowers the stiffness of the beam, and lowers the predicted resonance frequencies. The Timoshenko beam equation has the following form:[34]

$$EI\frac{\partial^4 u}{\partial y^4} + \omega^2\rho I\left(1 + \frac{EA_m}{A_e Gk}\right)\frac{\partial^2 u}{\partial y^2} = \omega^2\rho A_m\left(1 - \frac{\omega^2\rho I}{A_e Gk}\right)u, \quad (4)$$

where G is the shear modulus and k is the Timoshenko shear coefficient, which depends on the geometry. Normally $k = 9/10$ for circular cross sections. The appearance of the cross section of the tube in Eq. (4) originates from two different sources: A_m derives from the force balance equation, whereas A_e is a cross section originating from the elastic stress-strain constitutive relation.[34] Therefore, $A_m = 2\pi Rh_m$ and $A_e = 2\pi Rh_e$. Since the total mass per unit length for each tube in the simulation, $m = A_m\rho$, is known, one can replace ρ by m/A_m and has the freedom to chose $h_m = 3.4$ Å.

After replacing ρ by m/A_m and changing to the dimensionless parameter $\xi = y/L$, Eq. (4) transforms into

$$\frac{\partial^4 u}{\partial \xi^4} + \frac{\omega^2 mL^2}{A_m E}\left(1 + \frac{EA_m}{A_e Gk}\right)\frac{\partial^2 u}{\partial \xi^2} = \frac{\omega^2 mL^4}{EI}\left(1 - \frac{\omega^2 mI}{A_m A_e Gk}\right)u, \quad (5)$$

which has the same form as Eq. (2) with the following assignments:

$$\frac{1}{p^2} = \frac{\omega^2 mL^2 10^{-3}}{A_m E}\left(1 + \frac{EA_m}{A_e Gk}\right), \quad (6)$$

$$\beta^4 = \frac{\omega^2 mL^4 10^{-3}}{EI}\left(1 - \frac{\omega^2 mI 10^{-3}}{A_m A_e Gk}\right), \quad (7)$$

where ω is in THz; m is in fg; L, R, h_e, h_m are in nm; and E and G are in TPa.

One may observe that Eq. (5) has the same structure as Eq. (2) for $T_0 = -|T_0|$, which means that the beam is under compression, and as a result the resonance frequencies will be smaller than the f_n^0, given by Eq. (3). Before solving Eq. (5) let us first examine Eq. (2). This equation has an analytical solution for $T \neq 0$ as well; however the expression is quite cumbersome, but may be defined in the following relation, $\beta_n = \mathcal{F}(TL^2/EI) = \mathcal{F}(p^2)$ where $T = -T_0 > 0$. For $q = 1/p \to 0$ $\beta_n \to \beta_n^0$, hence we can expand $\mathcal{F}(p^2)$ for small q. Up to second order in p one finds

$$\beta_n \simeq \beta_n^0 - \frac{\alpha_n}{p^2} = \beta_n^0 - \alpha_n\frac{TL^2}{EI}, \quad (8)$$

where $\alpha_n = 0.029, 0.024, 0.019, 0.015$ for modes $n = 1$–4, respectively. Equation (8) demonstrates how the vibrational mode frequencies decrease as the beam is subjected to a compressive load, T. From a Taylor expansion one has $\beta_n - \beta_n^0 \simeq \frac{\partial\beta_n}{\partial\omega}\delta\omega$, and together with Eqs. (6), (7), and (8) one obtains

$$\delta\omega_n = \omega_n - \omega_0^n = -\frac{\alpha_n}{p^2\partial\beta_n/\partial\omega}$$
$$= -2\alpha_n\left(\beta_n^0\right)^3\omega_n^0\frac{I}{L^2 A_m}\frac{1 + \frac{EA_m}{GkA_e}}{1 - \frac{2\omega_n^0 mI}{A_m A_e Gk}}. \quad (9)$$

For $\sigma = R/L \ll 1$, $h_e = 0.66$ Å $< h_m = 3.4$ Å and $G = E/2(1 + \nu)$ as anticipated for a homogenous material, and Eq. (9) becomes

$$\delta\omega_n = -2\alpha_n\left(\beta_n^0\right)^3\omega_n^0\frac{EI}{L^2 GkA_e} \simeq -\alpha_n\left(\beta_n^0\right)^3\omega_n^0\frac{R^2}{L^2}\frac{E}{kG}, \quad (10)$$

where the last approximation is justified when $h_e \ll R$, which is usually the case. After substitution of all the relevant coefficients in Eq. (10) one finds

$$\delta\omega_n = -C_n\omega_1^0\left(\frac{\beta_n^0 R}{\beta_1^0 L}\right)^2\frac{E}{kG}, \quad (11)$$

where $C_n = 3.07, 11.67, 25.32$, and 44.20 for modes $n = 1$–4, respectively. Equation (11) predicts the following: (i) The shift of the resonance frequencies is negative and it scales as $\sigma = R/L$ as expected. (ii) The shift increases for higher vibrational
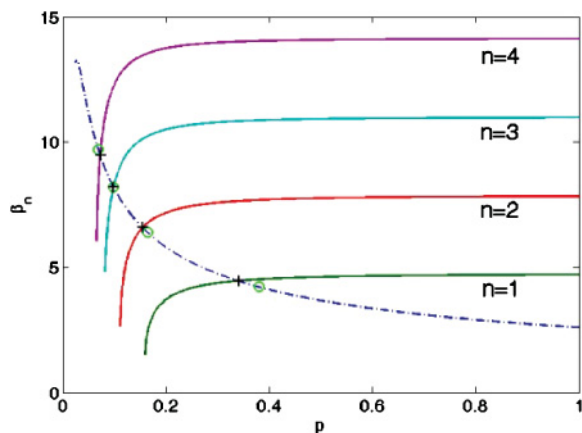
FIG. 5. (Color online) Fitting procedure. The four continuous colored lines represent the solutions of Eq. (2), i.e., $\beta_n = \mathcal{F}(p)$, for the first four vibrational modes. The blue dashed-dot line satisfies Eq. (12), i.e., $\beta = \mathcal{V}(p)$. The solutions for Eq. (5) are the intersection points between these lines (black plus signs). The fitting procedure minimizes the absolute distance between these intersection points with the simulated data (green circles).

modes. (iii) $\delta\omega_n/C_n/\omega_n^0 \propto (R/L)^2$ and the proportionality coefficient is $\frac{E}{kG}$. The simulated data agree very well with these predictions, and indeed linear dependence of $\delta\omega_n/C_n/\omega_n^0$ versus $(R/L)^2$ is found with coefficient $\frac{E}{kG} = 3.5 \pm 0.5$ for small $\sigma = R/L$. Assuming $k \simeq 0.9$, one gets $E/G \simeq 3.15 \pm 0.45$ which is in good agreement with $E/G = 2(1 + \nu) = 2.8$ for homogenous material. Knowing the ratio of E/kG leaves us with two variables, h_e and E. The following procedure was used in order to find the eigenvalues ω_n of Eq. (5) that correspond best to the simulated data.

The solution for Eq. (2) with double clamped beam boundary conditions can be written as $\beta_n = \mathcal{F}(p)$ and is plotted for the first four modes in Fig. 5 (colored continuous lines). One can notice that for $p > 1$ $\beta_n \to \beta_n^0$, meaning that the residual tension plays no major role. However, as p decreases, β_n decreases as well until $p \to p_{cr}(n)$ where beyond these points no solution for Eq. (2) exists. For example for the first mode $p_{cr}(n = 1) = 1/(2\pi) \simeq 0.16$, where after substituting the definition of p one receives $\mid T_{cr} \mid = 4\pi^2 \frac{EI}{L^2}$ which is the Euler-Bernoulli instability criteria for buckling. Next, we eliminate ω from Eqs. (6) and (7) and find

$$\beta_n = \left(\frac{A_m G A_e [L^2 p^2 (A_m E + A_e G) - EI]}{I p^4 (A_m E + A_e G)} \right)^{1/4} = \mathcal{V}(p). \tag{12}$$

Solutions to Eq. (5) are found from the intersection points of $\beta = \mathcal{V}(p) = \mathcal{F}(p)$. Figure 5 depicts four intersection points (black plus signs) for the first four modes with Eq. (12) (blue dashed-dot line) for $E = 5.5$ TPa and $h_e = 0.47$ Å. The fitting procedure modifies only E and h_e in order to minimize the distance in the β-p plane between the eigenvalues of Eq. (5) (black plus signs) and the simulated frequencies (green circles). The minimization is perform using all the simulated data points with two fitting parameters (E, and h_e), and the results are depicted in Figs. 6 and 7. The continuous lines
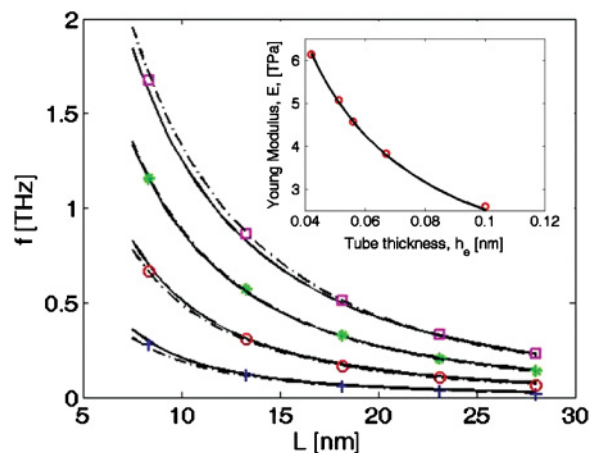

FIG. 6. (Color online) Main panel: First four vibrational modes as a function of length. The plus signs, circles, asterisks, and squares are for modes 1–4, respectively, continuous lines are derived from Eq. (5) with $E = 3.5$ kG $= 3.83$ TPa and $h_e = 0.67$ Å, and dashed-dot lines are solutions for the same equation with the same bending and shear rigidities but with $0.4 \leqslant h_e \leqslant 0.6$ Å. Inset: Possible solutions for Eq. (5) are marked by circles in the E-h_e plane and the continuous line corresponds to $Eh_e = 246$ GPa · nm.

are based on the theoretical model, and the discrete points are the simulated data. Young's modulus is calculated to be $E = 3.83$ TPa, and the tube thickness is $h_e = 0.67$ Å. These values match those found in Huang *et al.*[22] For the data of f versus L the agreement between experiment and theory is excellent. This is expected since for this data set, the maximum value of $\mu = R/\lambda_n = 0.11$ which is smaller than the maximum, $\mu = 0.22$, of the other set. However, in the case of the second set of data, f versus R, the model matches the simulated data quite well, and the "roll off" of the resonance frequencies for larger radii are well observed.
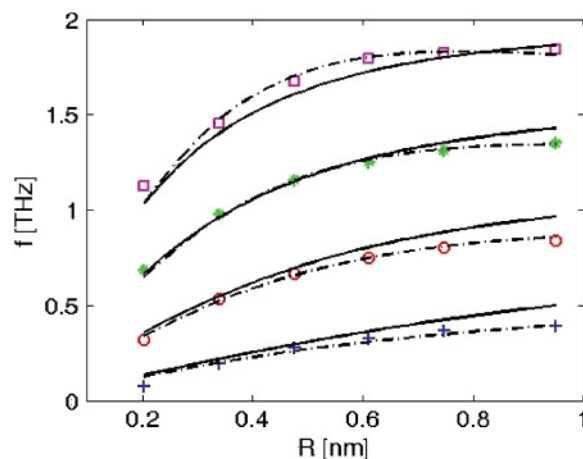

FIG. 7. (Color online) First four vibrational modes as a function of radius. The plus signs, circles, asterisks, and squares are for modes 1–4, respectively, continuous lines are derived from Eq. (5) with $E = 3.5$ kG $= 3.83$ TPa and $h_e = 0.67$ Å, and dashed-dot lines are solutions for the same equation with the same bending and shear rigidities but with $0.4 \leqslant h_e \leqslant 0.6$ Å.

Three fundamental questions arise with regard to these findings: (i) Why do the resonance frequencies almost saturate for big radii? (ii) Can we extract E and h_e uniquely? (iii) In light of several studies that predict that the tension rigidity, $(Eh_e)/(1 - \nu^2)$ depends on radii, how do the above results change if one allows for the tension rigidity to be varied slightly?

Let us start with the first question. By examining Eq. (6) and substituting ω_n^0 one finds

$$\frac{1}{p^2} \simeq (\beta_n^0)^4 \left(\frac{R}{L}\right)^2 \frac{E}{2Gk}. \tag{13}$$

Hence, as the radius increases and/or the vibrational modes under consideration become larger, p becomes smaller, the effective compression is stronger, and as a result the beam approaches its critical buckling singularity points. Thus, the beam becomes softer and the anticipated resonance frequencies are reduced in comparison with f_n^0. Since a SWCNT can be considered in the framework of the shell model, local as well as global buckling are predicted.[15] These local buckling instabilities can affect the circular cross section[33] and hence modify the bending and shear rigidities. If one allows for the effective tube thickness (h_e) to be modified slightly with radius but keeps the same Young's and shear moduli as were found before (Figs. 7 and 6) excellent agreement between the model and simulated data is also obtained for the f versus R data (dashed-dot lines in Figs. 6 and 7). The overall modification of the tube thickness was small (between 0.6 Å for the small radius and 0.4 Å for the thickest tube); however, its influence on the fitted data is significant, mainly for the high μ points.

We have also been concerned about the issue of the origin of the radius dependence of the shell thickness. Of course this is of quantum mechanical origin, and members of our group have considered this in the context of both nanotubes and other carbon allotropes. In a recent paper[35] the authors compare an *ab initio* study (with VASP) of electronic density of sp_2 and sp_3 bonds with classical potential studies of sp_2/sp_3 diamond samples. The Brenner potential is indeed classical but is parametrized well enough to give correct results for atomic locations when is compared with the VASP results. To get the actual electronic density widths one needs to rely on *ab initio* calculations.

Figures 7 and 6 show good agreement between experiment and theory for $E = 3.83$ TPa and $h_e = 0.67$ Å. Are these values are unique, or may one find other values with similar matching? As has been discussed by many experimentalists and theoreticians in this field, and known as Yakobson's paradox, the combination of $Y = Eh_e$ is the quantity that is usually measured and studied. Despite the big scattering in the values of E and h_e that have been published in the literature and may be dependent on loading as well,[22] the distribution of Y is quite sharp and it is centered around 246 GPa · nm. From the Timoshenko beam model, one can observe from Eqs. (5), (6), and (7) that $\frac{1}{p^2} \propto \frac{\omega^2}{h_e E}$ and $\beta^4 \propto \frac{\omega^2}{h_e E}(1 - a\frac{\omega^2}{G})$. Thus, for $a\frac{\omega^2}{G} \ll 1$, the same paradox will appear for this model. However, as μ and ω increase this term becomes larger and therefore partially resolves Yakobson's paradox. Specifically, the possible solutions for E and h_e according to the presented model in the E-h_e plane are depicted in the inset of Fig. 6. They indeed fulfill the condition of $Eh_e = \text{const} = 246$ GPa · nm (continuous line) but $h_e = 3.4$ Å is beyond this range.

V. CONCLUSIONS

In summary, we presented a detailed atomistic molecular dynamics simulation and analysis of the thermal vibrational modes of SWCNTs within the Brenner interatomic potential. The simulation spans substantial range of tube length and radii, and agrees well with the Euler-Bernoulli continuum beam model for small $\mu = R/\lambda$ ratios. However, for bigger μ the data deviate significantly from the predicted model, and an alternative model (known as the Timoshenko model) that takes into account the effects of rotary inertia and shearing deformation was adopted. The new model agrees well with the simulated data, and the reduction of the eigenvalues of the vibrational modes was attributed to softening of the tube by compression close to global or local buckling instabilities. The results of this study may be relevant also for the design of high frequency NEMS based on SWCNTs. In contradiction to common belief that as the tube becomes shorter, or thicker, the resonance frequencies increase, the simulation and the model emphasize the significance of the dimensionless parameter μ and show that for $\mu > 0.05$ the resonance frequencies are much lower than expected.

*yuvaly@ee.technion.ac.il

[1] R. Ruoff and D. Lorents, Carbon **33**, 925 (1995).

[2] D. Srivastava, M. Menon, and K. Cho, Comput. Sci. Eng. **3**, 42 (2001).

[3] V. Sazonova, Y. Yaish, H. Ustunel, D. Roundy, T. A. Arias, and P. L. McEuen, Nature (London) **431**, 284 (2004).

[4] A. K. Huttel, G. A. Steele, B. Witkamp, M. Poot, L. P. Kouwenhoven, and H. S. J. van der Zant, Nano Lett. **9**, 2547 (2009).

[5] B. Lassagne, D. Garcia-Sanchez, A. Aguasca, and A. Bachtold, Nano Lett. **8**, 3735 (2008).

[6] H.-Y. Chiu, P. Hung, H. W. C. Postma, and M. Bockrath, Nano Lett. **8**, 4342 (2008).

[7] K. Jensen, K. Kim, and A. Zettl, Nature Nanotechnol. **3**, 537 (2008).

[8] M. Treacy, T. Ebbesen, and J. Gibson, Nature (London) **381**, 678 (1996).

[9] P. Poncharal, Z. Wang, D. Ugarte, and W. de Heer, Science **283**, 1513 (1999).

[10] M. Xia, S. Zhang, E. Zhang, S. Zhao, and X. Zuo, Phys. Rev. B **69**, 233407 (2004).

[11] J. Yoon, C. Ru, and A. Mioduchowski, Composite Sci. Technol. **63**, 1533 (2003).

[12] K. Sohlberg, B. Sumpter, R. Tuzun, and D. Noid, Nanotechnology **9**, 30 (1998).

[13] G. Cao, X. Chen, and J. W. Kysar, Phys. Rev. B **72**, 235404 (2005).

[14] J. Tersoff, Phys. Rev. B **46**, 15546 (1992).

[15] B. I. Yakobson, C. J. Brabec, and J. Bernholc, Phys. Rev. Lett. **76**, 2511 (1996).

[16] C. Q. Ru, Phys. Rev. B **62**, 9973 (2000).

[17] C. Li and T. Chou, Int. J. Solids Struct. **40**, 2487 (2003).

[18] C. To, Finite Elements in Analysis and Design **42**, 404 (2006).

[19] Y. Jin and F. G. Yuan, Compos. Sci. Technol. **63**, 1507 (2003).

[20] L. Wang, Q. Zheng, J. Z. Liu, and Q. Jiang, Phys. Rev. Lett. **95**, 105501 (2005).

[21] O. A. Shenderova, V. V. Zhirnov, and D. W. Brenner, Crit. Rev. Solid State Mater. Sci. **27**, 227 (2002).

[22] Y. Huang, J. Wu, and K. C. Hwang, Phys. Rev. B **74**, 245413 (2006).

[23] C. Y. Wang and L. C. Zhang, Nanotechnology **19**, 195704 (2008).

[24] D. W. Brenner, Phys. Rev. B **42**, 9458 (1990).

[25] D. W. Brenner, J. A. Harrison, C. T. White, and R. Colton, Thin Solid Films **206**, 220 (1991).

[26] J. A. Harrison, S. J. Stuart, D. H. Robertson, and C. T. White, J. Phys. Chem. B **101**, 9682 (2005).

[27] S. B. Sinnot, R. J. Colton, C. T. White, O. A. Shenderova, D. W. Brenner, and J. A. Harrison, J. Vac. Sci. Technol. A **153**, 936 (1997).

[28] J. Adler, A. Hashibon, N. Schreiber, A. Sorkin, S. Sorkin, and G. Wagner, Comput. Phys. Commun. **147**, 665 (2002).

[29] H. Berendsen, J. Postma, W. van Gunsteren, A. DiNola, and J. Haak, J. Chem. Phys. **81**, 3684 (1984).

[30] J. Sudark, J. Appl. Phys. **94**, 7281 (2003).

[31] L. D. Landau and E. M. Lifshitz, *Elasticity Theory* (Pergamon, Oxford, 1986).

[32] S. P. Timoshenko and J. N. Goodier, *Theory of Elasticity*, 3rd ed. (McGraw Hill, New York, 1987).

[33] D. Srivastava, C. Wei, and K. Cho, Appl. Mech. Rev. **56**, 215 (2003).

[34] S. P. Timoshenko, D. H. Young, and J. W. Weaver, *Vibration Problems in Engineering*, 4th ed. (John Wiley and Sons, New York, 1974).

[35] J. Adler, J. Zaffran, A. Silverman, A. Sorkin, O. Cohen, and R. Kalish, Comput. Phys. Commun. (to be published 2011).